Purdue University
Purdue e-Pubs

Birck and NCN Publications | Birck Nanotechnology Center

April 2008

Building semiconductor nanostructures atom by atom

M Korkusinski
Institute for Microstructural Sciences, National Research Council

P Hawrylak
Institute for Microstructural Sciences, National Research Council

M Zielinski
Institute for Microstructural Sciences, National Research Council

W Sheng
Department of Physics, Fudan University

Gerhard Klimeck
Network for Computational Nanotechnology, Purdue University, gekco@purdue.edu

Follow this and additional works at: http://docs.lib.purdue.edu/nanopub

Korkusinski, M; Hawrylak, P; Zielinski, M; Sheng, W; and Klimeck, Gerhard, "Building semiconductor nanostructures atom by atom" (2008). *Birck and NCN Publications.* Paper 176.
http://docs.lib.purdue.edu/nanopub/176

This document has been made available through Purdue e-Pubs, a service of the Purdue University Libraries. Please contact epubs@purdue.edu for additional information.

ELSEVIER

Microelectronics Journal 39 (2008) 318–326

Microelectronics Journal

www.elsevier.com/locate/mejo

Building semiconductor nanostructures atom by atom

M. Korkusinski[a,*], P. Hawrylak[a], M. Zielinski[a], W. Sheng[a,b], G. Klimeck[c]

[a]Institute for Microstructural Sciences,National Research Council, Ottawa, Canada K1A 0R6
[b]Department of Physics, Fudan University, Shanghai 200433, China
[c]Network for Computational Nanotechnology, Purdue University, West Lafayette, IN 47907, USA

Available online 20 August 2007

Abstract

We present an atomistic tight-binding approach to calculating the electronic structure of semiconductor nanostructures. We start by deriving the strain distribution in the structure using the valence force field model. The strain field is incorporated into the tight-binding electronic structure calculation carried out in the frame of the effective bond orbital model and the fully atomistic $sp^3d^5s^*$ approach. We apply the method to a vertically coupled self-assembled double-dot molecule. Using the effective mass approach, we establish the existence of electronic bonding and antibonding molecular orbitals for electrons and holes, whose probability density is shared equally between the dots. In the atomistic calculation we recover the molecular character of electron orbitals, but find that structural and atomistic details of the sample modify the hole orbitals, leading to a strongly asymmetric distribution of the probability density between the dots.
© 2007 Elsevier Ltd. All rights reserved.

Keywords: Atomistic calculations; Tight-binding model; Artificial molecule

1. Introduction

Self-assembled InAs/GaAs quantum dot (QD) nanostructures are typically composed of $\sim 10^7$ atoms [1]. The single dots typically assume the shape of a lens, disk, or pyramid, with characteristic lateral dimensions of several tens of nanometers, and heights of several nanometers [1–3]. The dots can be further vertically stacked, leading to the formation of self-assembled QD molecules [4–7]. The composition profile of these structures, i.e., distribution of atoms of the quantum barrier and well material in the volume of the sample, translates into the spatial confinement of electrons and holes. As a consequence, the electronic and optical properties of the dots and dot molecules could, in principle, be completely characterized in a full quantum-mechanical treatment, involving all atomic nuclei and all electrons present in the sample. Such treatment, however, is beyond our current computational abilities, and approximate approaches have to be used in order to understand the fundamental physics of nanostructures.

In the simplest treatment the electrons and holes are considered as elementary excitations with effective mass, interacting via Coulomb interactions, and confined, respectively, by the conduction and valence band offsets of the materials composing the sample. This model allowed for a good qualitative understanding of the main features appearing in optical spectra, measured both for single [8–11] and double dots [5,6], and accounts for the characteristic shell structure and crossings of levels even at very high magnetic fields [12]. However, high-resolution single-dot photoluminescence (PL) studies reveal additional properties, which cannot be fully treated within this single-band effective mass approach. In the measurements of the Stark shift of PL peaks in an electric field, Finley et al. [13] detected permanent electron–hole dipoles, indicating that the distribution of Indium atoms is not uniform in the volume of the alloyed InGaAs dots. Klimeck et al. [14] have demonstrated theoretically that the properties of such systems are also sensitive to the alloy disorder effects. Further, the fine structure of confined excitons was detected [15], indicating the presence of electron–hole

*Corresponding author.
E-mail address: marek.korkusinski@nrc.ca (M. Korkusinski).

0026-2692/$ - see front matter © 2007 Elsevier Ltd. All rights reserved.
doi:10.1016/j.mejo.2007.07.016

exchange. Proper treatment of these effects requires knowledge of microscopic details of carrier wave functions. Moreover, the subband mixing effects are responsible for coupling of the carrier spin and orbital degrees of freedom, leading to a dependence of the excitonic g factor on the size and shape of the dots [16]. The structural and optical properties of the dots are also influenced by the symmetry of the zincblende crystal lattice of the sample. Bayer et al. [17] demonstrated that the [1 1 0] or $[1\,\bar{1}\,0]$ crystallographic directions are preferred as symmetry axes of the ellipsoidal dots, and that the emitted PL light is polarized linearly along them. In single dots, the lack of inversion symmetry of the lattice may lead to a removal of single-particle degeneracies, and in particular a splitting of the p shell states [18]. As we shall show later on, in the case of dot molecules the lack of inversion symmetry of the lattice introduces an overall asymmetry of the system even if the dots composing it are identical [19,20]. In order to bring the dots into resonance, the structural asymmetry has to be compensated, e.g., by applying an external electric field [21].

These examples demonstrate a need for the theoretical method of computing the electronic properties of nanostructures which treats the details of geometry, composition, and strain on an atomistic level. As already mentioned, the large number of atoms involved prevents us from employing the methods that consider all electrons and nuclei present in the system, such as configuration–interaction or density functional theory. Instead, we use approximate approaches, in which the energies and wave functions of an excitation (a quasielectron or a quasihole) are computed in a basis of orbitals localized on atoms. These approaches can be divided into two groups. In the empirical pseudopotential methods [19,22] one attempts to derive the basis orbitals by assuming that the nucleus and all core electrons localized on each atom contribute to a single-particle pseudopotential in its vicinity. In this work, however, we focus on the atomistic tight-binding approach, in which the atomic basis is never completely defined, but the Hamiltonian matrix elements describing the coupling of neighboring atoms are treated as fitting parameters. Since the QD nanostructures are highly strained, the necessary first step is to establish the equilibrium positions of all atoms. The atomic displacements influence the energy diagram of the structure by rescaling the tight-binding parameters. The full tight-binding Hamiltonian is further written as a very large, but sparse matrix, and diagonalized using iterative methods. As an example, we use two tight binding methods—the effective bond orbital model (EBOM) and the atomistic $sp^3d^5s^*$ approach—to calculate the electronic structure of artificial molecules composed of two and seven vertically coupled QDs.

2. Atomistic calculation of strain

As already mentioned, a prerequisite for the atomistic calculation of the electronic structure is the knowledge of atomic positions. Since the lattice constant of the InAs QD is ~7% larger than that of the GaAs barrier material, the equilibrium positions of atoms composing the nanostructure will be displaced from those in the bulk, and these displacements will vary across the sample. As a result, the lengths and directions of atomic bonds become distorted, which influences the energy diagram of the system. Two approaches, commonly used to find the displacement field, involve minimization of the total elastic energy of the nanostructure. In the continuous elasticity theory [23,24] this elastic energy is defined as a sum of local distortions of a continuous medium discretized on a computational grid. Here, however, we use the atomistic approach of Keating [25], in which the total elastic energy E_{TOT} contains the stretching and bending terms from each atomic bond in the system:

$$E_{\mathrm{TOT}} = \frac{1}{2}\sum_{i=1}^{N}\sum_{j=1}^{\mathrm{n.n.}} A_{ij}[(\vec{R}_i - \vec{R}_j)^2 - d_{ij}^2]^2 + \sum_{i=1}^{N}\sum_{j=1}^{\mathrm{n.n.}}\sum_{k=j+1}^{\mathrm{n.n.}} B_{ijk}[(\vec{R}_j - \vec{R}_i)\cdot(\vec{R}_k - \vec{R}_i) - \frac{1}{3}d_{ij}d_{ik}]^2. \tag{1}$$

Here, $\vec{R}_i$ denotes the position of the ith atom, d_{ij} is the bulk bond length between the ith and jth atoms, and A_{ij} and B_{ijk} are material-dependent elastic parameters. The summations go over N atoms and n.n. nearest neighbors. To obtain the displacement field we minimize this energy with respect to the atomic positions using the conjugate gradient algorithm. The distribution of strain tensor elements across the sample is then computed by comparing the deformed zincblende unit cells with their unstrained bulk counterparts [24]. Once the shear strain matrix elements are known, we can calculate the piezoelectric charge $\varrho_{\mathrm{P}}(x,y,z)$ induced in the sample [26]. The piezoelectric potential, obtained by solving the Poisson equation with ϱ_{P}, is then added to the electronic Hamiltonian of the system.

We have performed a detailed analysis of the properties of the strain field present in the sample containing a single QD as a function of the number of atoms making up the computational domain and the boundary conditions taken at its edges [27]. We have found that the range of the strain field is very long: the existence of boundaries influenced the field inside the dot even when the dimensions of the computational domain were $120 \times 120 \times 60$ nm, i.e., more than an order of magnitude larger than the dimensions of the dot. Also, the strain field is strongly anisotropic, as it decays along the z-axis much slower than it does in the QD plane. This effect is responsible for the self-alignment of the QD stacks in the growth process.

3. Atomistic tight-binding electronic structure calculations

Once the equilibrium atomic positions are established, we can move on to calculating the electronic structure of

the system. To this end we use two tight-binding approaches: the EBOM and the atomistic 20-band $sp^3d^5s^*$ calculation. Both treatments involve writing the single-particle Hamiltonian of the system on a lattice of N sites in the form

$$\hat{H}_{TB} = \sum_{i=1}^{N} \sum_{\alpha=1}^{NB} E_{i\alpha} c_{i\alpha}^{+} c_{i\alpha} + \sum_{i=1}^{N} \sum_{j=1}^{\text{n.n}} \sum_{\alpha,\beta=1}^{NB} t_{i\alpha,j\beta} c_{i\alpha}^{+} c_{j\beta}, \tag{2}$$

where $c_{i\alpha}^{+}$ ($c_{i\alpha}$) is the creation (annihilation) operator of a carrier on the orbital α localized on the site i, $E_{i\alpha}$ is the corresponding onsite energy, and $t_{i\alpha,j\beta}$ describes the hopping of the particle between orbitals localized on the same or neighboring sites. Here we assume that each site holds NB orbitals and is surrounded by n.n. neighbors.

3.1. The $sp^3d^5s^*$ approach

Here the sites are identified as atoms forming the zincblende lattice. Each atom has n.n. = 4 nearest neighbors, and holds 20 spin degenerate orbitals: 2 of type s, 6 of type p, 10 of type d, and 2 of type s^*. Let us briefly discuss the derivation of tight-binding matrix elements, assuming that an s orbital is placed on the atom i, and a p_z orbital on the atom j, and that atoms i and j are nearest neighbors. If the two orbitals have different spin, the matrix element is zero. For the orbitals of the same spin we use the notation put forward by Vogl et al. [28] for the sp^3 model. In this approach all matrix elements are assumed to depend only on the relative positions of the atoms i and j, with all three-center and higher contributions neglected. Also, the matrix elements are expressed in terms of the simple cubic lattice constants of the form $V_{\alpha\beta\sigma}$ and $V_{\alpha\beta\pi}$, where in our case the orbitals $\alpha \equiv s$ and $\beta \equiv p_z$, and σ and π denote the symmetry of the bond. If the two atoms are connected by a bond of the [1 0 0] type, i.e., the axis connecting them is parallel to the x-axis, the orbitals s and p_z create a π bond and element $V_{s,p_z\pi} = 0$ because of the symmetry. On the other hand, if the direction of the bond is [0 0 1], i.e., vertical, then the bond is of a σ type and the element $V_{s,p_z\sigma}$ is finite. However, in our systems we deal with a zincblende lattice, in which the nearest neighbors are connected by bonds $\vec{d} = |d|(l\hat{x} + m\hat{y} + n\hat{z})$, with d being the bond length and l, m, n—the direction cosines. Here, expressing the tunneling element in terms of cubic constants involves projecting the p_z orbital onto the bond and in the direction perpendicular to it. Since the perpendicular projections give π-type bonds, their contribution is zero. The Hamiltonian matrix element is thus $t_{i,s,j,p_z} = nV_{sp\sigma}$. All matrix elements of our Hamiltonian are expressed in a similar fashion according to the so-called Slater–Koster rules [29]. This notation is particularly convenient in introducing the strain effects into the model. Since the atomic displacements result in the change of the bond direction (bond bending) and its length (bond stretching), the Hamiltonian matrix element under strain takes the form $t_{i,s,j,p_z} = n'V_{sp\sigma}(d_{ij}/d_0)^{\eta}$, where n' is the new directional cosine of the bond. The ratio of the new to old (ideal) bond length d is scaled by the exponent η, whose value is usually close to 2 [30]. Finally, the spin-orbit interaction is accounted for by introducing finite matrix elements Δ connecting orbitals of opposite spin, residing on the same atom. For example, $\langle i, p_y, \uparrow |H| \downarrow, p_z, i\rangle = -\mathrm{i}\Delta$.

The values of the tight-binding parameters are established by fitting the gaps and effective masses in the bulk band structure obtained with the model at high symmetry points of the Brillouin zone to the values established experimentally. The most frequently used parametrizations are given in Refs. [31,32]. In this work we use the NEMO3D parametrization of Klimeck et al. described in detail in Refs. [14,32,33]. These parametrizations demonstrate that the inclusion of d orbitals into the basis allows to obtain much better fits of the masses and energy gaps to the target material values. In particular, the treatment of the conduction band edge is significantly improved, which is particularly important for small nanostructures [34].

The last problem to address is the treatment of the interface. In the InAs/GaAs defect-free system, the In and Ga atoms are always surrounded by As atoms, but the nearest neighbors of As atoms may differ. Therefore it is not necessary to introduce the constants describing Ga–In bonds, as in our case such bonds are not realized. To account for the interface we perform weighted averaging of the hopping parameters in a manner that reflects the composition of the neighborhood of each As atom. Also, the diagonal Hamiltonian elements are modified to account for the band offset between the materials forming the interface. The second type of interface arises on the edges of the computational domain. There, the appearance of free surfaces leads to the dangling bonds, whose energy falls in the interior of the semiconductor gap of the barrier. A passivation procedure, described in Ref. [35], is performed in order to shift the surface-localized states away from the region of energies corresponding to confined QD orbitals.

3.2. The EBOM model

The atomistic tight-binding model described in the previous section is formulated in the basis, whose size is $20N$, with N being the total number of atoms in the simulation space. In the EBOM, on the other hand, the actual zincblende crystal lattice of the materials is replaced by a single FCC lattice of effective sites [36]. In this case each site has 12 nearest neighbors, and holds four spin-degenerate effective orbitals: one of type s and three of type p, resulting in the basis of only $5N$ effective orbitals. The effective lattice does not reflect the complete crystal symmetry of the system, but is more manageable computationally and may be used in preliminary calculations. The tight-binding parameters appearing in the EBOM approach are written in terms of the Slater–Koster rules appropriate for the FCC lattice. Their values can be obtained by extrapolating the EBOM model applied to the bulk to the $\vec{k} \cdot \vec{p}$ approach close to the Γ point. As a result,

all energy constants can be expressed in terms of the characteristic gaps, effective masses, and Luttinger parameters. Due to the simplified lattice, the effects of strain are incorporated in an indirect manner by constructing the Bir–Pikus Hamiltonian from the position-dependent strain tensor elements multiplied by the deformation potentials [23,37]. The total Hamiltonian matrix is formed as a sum of the EBOM and Bir–Pikus Hamiltonians.

4. Application of tight-binding models to artificial molecules

Let us now apply the tight-binding methods to a vertically coupled InAs double-dot molecule embedded in the GaAs barrier material. The system, shown schematically in Fig. 1(a), is composed of two identical quantum disks (QDs) of radius $R = 8\,\text{nm}$ and height of $H = 2\,\text{nm}$, separated by a barrier of thickness D, and sharing a common axis of rotational symmetry.

4.1. Effective-mass analysis

The simplest insight into the properties of the system is obtained in the single-band effective mass approach, in which the material parameters of the QDs enter through the effective Rydberg, $\mathcal{R} = m_e^* e^4/2\varepsilon^2\hbar^2$, and the effective Bohr radius $a_\text{B} = \varepsilon\hbar^2/m_e^* e^2$, with e, m_e^* being, respectively, the electronic charge and effective mass and ε—the dielectric constant of the material. We take the GaAs value of $\varepsilon = 12.4$, and treat the effective masses of the electron and the hole as fitting parameters of the model. The second parameter, $V_0^{e(h)}$, describes the depth of the QD confinement, and is established for the electron and the hole as the offset of the conduction and valence band edges, respectively.

Let us first assume that in the absence of the tunneling coupling each dot holds one electron and one hole orbital. We denote the electronic orbital in the top (bottom) dot as $\phi^e_{\text{T(B)}}(\vec{r})$, and its energy as $E^e_{\text{T(B)}}$, while the corresponding orbitals for holes are denoted as $\phi^h_{\text{T(B)}}(\vec{r})$, with corresponding energies $E^h_{\text{T(B)}}$. For each carrier type these orbitals can be mapped onto the isospin states, such that the state $|\uparrow\rangle$ denotes the particle localized in the top dot, and the state $|\downarrow\rangle$—in the bottom dot. The interdot tunneling can be modeled by the hopping parameter $t>0$, such that the single-particle electronic Hamiltonian written in the basis of the isospin states $\{|\downarrow\rangle, |\uparrow\rangle\}$ takes the form

$$\hat{H}_t^e = \begin{bmatrix} E^e_\text{B} & -t^e \\ -t^e & E^e_\text{T} \end{bmatrix}. \tag{3}$$

The hole Hamiltonian has a similar form, but is scaled by the hole tunneling element t^h. If the disks are identical, $E^e_B = E^e_T = E^e_0$, and the ground state of the system is a bonding (symmetric) orbital $|+\rangle_e = (|\downarrow\rangle_e + |\uparrow\rangle_e)/\sqrt{2}$ with energy $E^e_+ = E^e_0 - t$. On the other hand, the first excited state is antibonding (antisymmetric), and takes the

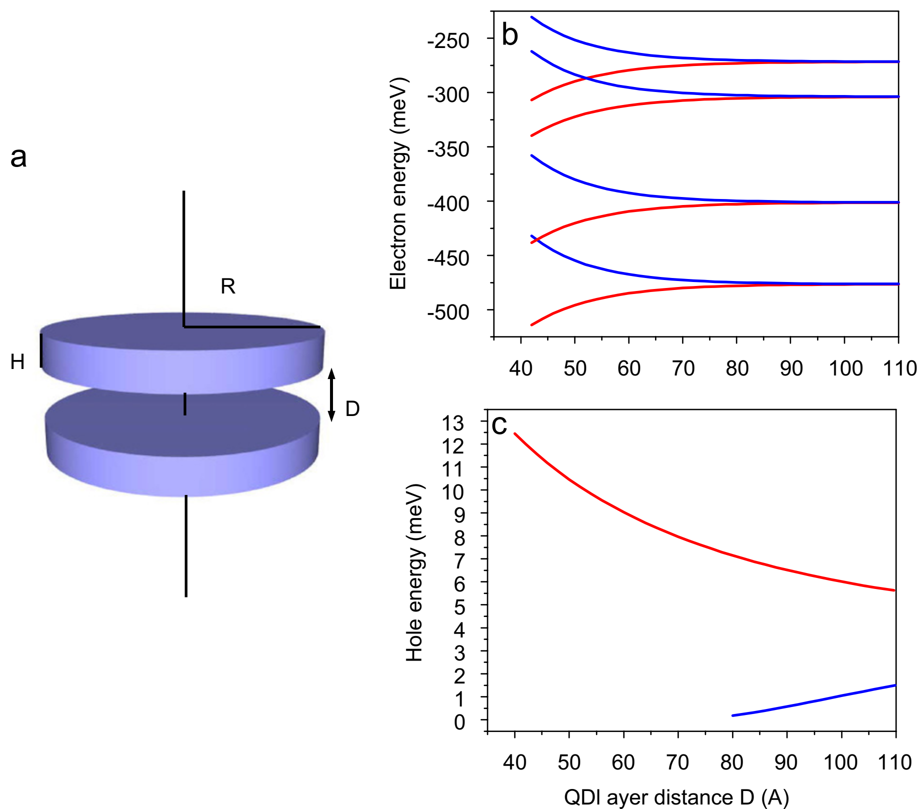

Fig. 1. (a) Schematic view of the vertically coupled double-dot molecule. Diagrams show the energies of electron (b) and hole (c) states calculated as a function of interdot separation D in the single-band effective mass approach. Red (blue) lines correspond to bonding (antibonding) orbitals.

form $|-\rangle_e = (|\downarrow\rangle_e - |\uparrow\rangle_e)/\sqrt{2}$ with energy $E^e_+ = E^e_0 + t$. A similar analysis can be carried out for the hole. Thus, the interdisk tunneling leads to rotations of the isospin states of both types of carriers. The magnitude of the element t, and thus the splitting between the bonding and antibonding state, depends on the distance D between the QDs.

In a more quantitative analysis we calculate the single-band energies of a single electron and a single hole confined in a potential $V(r,z) = -V^e_0$ inside, and 0 outside the QDs. In Ref. [38] we have solved for the eigenstates of the corresponding single-particle Hamiltonian as a function of the barrier thickness D using the semianalytical adiabatic approximation. In Fig. 1(b) and (c) we show, respectively the electron and hole energies calculated as a function of D using the unstrained InAs/GaAs band offset parameters of $V^e_0 = 1$ eV and $V^h_0 = 85$ meV [39], and the effective masses $m^*_e = 0.053\ m_0$ and $m^*_h = 0.1m_0$. As seen in Fig. 1(b), at large interdisk distances the two QDs are practically decoupled, and the electronic energy levels form degenerate shells. As the distance D is decreased, the tunneling coupling increases exponentially, leading to the formation of pairs of bonding and antibonding orbitals for each shell. Formation of the bonding and antibonding orbital is also seen for holes (Fig. 1(c)). However, due to the shallow hole confinement and the resulting small height of the tunneling barrier for holes the spectrum for small D consists only of the s-type bonding level. The corresponding antibonding state becomes confined only for distances D large enough, but even then the tunneling splitting is much larger than that for the electronic states at the same interdisk separation.

4.2. Strain effects

Let us now incorporate the strain effects into the energy diagram of the system. As already mentioned, this can be accomplished via the Bir–Pikus Hamiltonian. Here let us focus on its diagonal elements, containing contributions from two strain terms. The first term is the hydrostatic strain, ε_h, which describes the relative change of the volume of the strained unit cell. A detailed analysis [38] shows that this component is negative (compressive) across the sample, and assumes large values only inside the QDs. This term alone is responsible for the rescaling of the conduction band edges of the system, which, as shown in Fig. 2(a), leads to the reduction of the QD electronic confinement to about 600 meV. In the valence band the influence of strain is more complicated, as it leads to splitting and mixing of the hole subbands. Here, both heavy and light hole subbands acquire the same energy

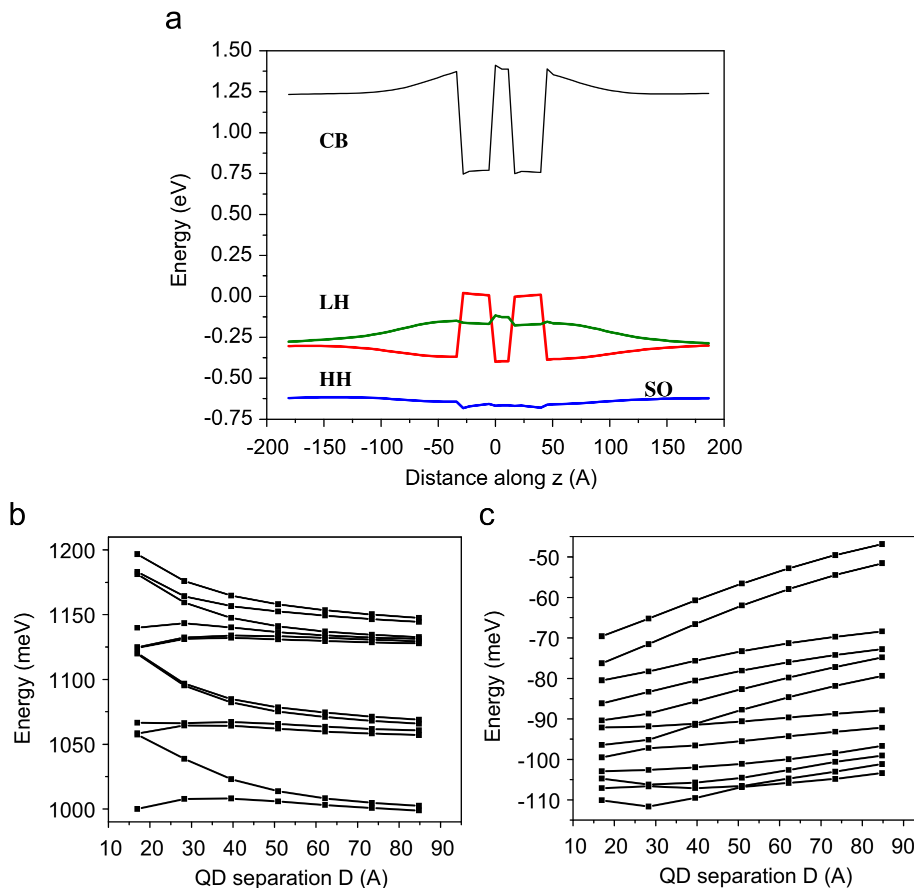

Fig. 2. (a) Conduction and valence band edges of a strained double-dot molecule computed using the Bir–Pikus Hamiltonian along the symmetry axis. Lower panel shows the electron (b) and hole (c) energies of the double-dot molecule as a function of the interdot separation D calculated using the EBOM model.

shift, $\Delta E_h = -a_v \varepsilon_h$, where the deformation potential $a_v = 0.66\,\text{eV}$ for InAs and 0.7 eV for GaAs [39]. In our system this leads to the increase of the confinement depth for the heavy holes to ~400 meV. Additionally, the energy of the heavy hole is renormalized by $\Delta E_b^{HH} = +b\varepsilon_b$, and that of the light hole by $\Delta E_b^{LH} = -b\varepsilon_b$, with the deformation potential $b = -1.8\,\text{eV}$ for InAs and $-2\,\text{eV}$ for GaAs, and the biaxial strain element $\varepsilon_b = \varepsilon_{zz} - \frac{1}{2}(\varepsilon_{xx} + \varepsilon_{yy})$. This element accounts for the anisotropy of the strain field of the system, and changes sign at the QD interface—from positive in the barrier to negative in the well [36]. Because the sign of the biaxial term in the heavy hole energy is opposite to that for light holes, we observe a splitting of valence subbands. On the other hand, at the QD interfaces the biaxial term changes sign, resulting in the reversal of the order of valence subbands on the band diagram of the system. In Fig. 2(a) this reversal is clearly seen as the band edges are plotted along the symmetry axis of the nanostructure. Note that the inclusion of the strain leads to an increase in the depth of the double-dot confinement of heavy holes, forming the topmost valence subband edge inside the QDs. On the other hand, the light holes are confined effectively in one, very broad quantum well, assuming a similar depth inside the QDs and across the GaAs buffer between them.

4.3. The EBOM approach

In the case of our double-dot molecule the order of the EBOM Hamiltonian matrix is of the order of $\sim 10^6$. This matrix, however, is sparse, and the orbitals confined within the nanostructure and their corresponding energies are found iteratively in the Lanczos procedure. The diagonalization is preceded by the computation of strain within a larger domain (of the order of eight million atoms) to account for the long-range character of the strain field. It is assumed that at the edges of this domain the atomic positions match those corresponding to the unstrained bulk material. We also incorporate the strain-induced piezoelectric potential. In Fig. 2(b) we show the energies of 12 lowest electron states, and in Fig. 2(c) those of the 12 lowest hole states as a function of the interdisk distance D [40]. The behavior of the electron energies is similar to that predicted in the effective-mass model: for small D we see the formation of bonding and antibonding states. Their energies are separated by a gap which decreases with the increase of D, and at large interdisk distances we recover a structure of nearly degenerate shells. The smaller curvature of the energies of bonding states and the increased curvature of the antibonding states as a function of D is due to the strain effects: as D increases, the interdisk barrier is less strained, resulting in a uniform downward shift of the entire energy spectrum. This behavior has been also detected in $\vec{k} \cdot \vec{p}$ calculations [23]. On the other hand, the behavior of the hole energies is very different than that predicted earlier. The two lowest hole states maintain an almost constant energy gap between them, and only shift in energy as D is increased. On closer inspection of the corresponding orbitals we find that the probability of finding a hole in the system is no longer equally shared between the two dots, but is localized predominantly in the bottom (the ground hole state) or top dot (the excited hole state). This behavior does not result from the FCC lattice of the EBOM model, because it possesses the inversion symmetry and does not break the overall vertical symmetry of the system. The symmetry breaking is introduced by the strain field, which has been calculated atomistically, i.e., using the actual zincblende lattice of the material.

4.4. Atomistic tight-binding approach

In this work we use the NEMO3D implementation of the $sp^3d^5s^*$ model. This software tool is written in C++ and parallelized for use on a Beowulf cluster using MPI for inter-CPU communication. It combines all elements of the tight-binding electronic structure calculation with the exception of piezoelectric effects. We apply this tool to our double-dot molecule, this time assuming that the two disks are not identical. The radius of the bottom disk is taken as $R_1 = 6.5\,\text{nm}$ while that of the top disk is $R_2 = 7\,\text{nm}$. Both disks have height of $H = 2.5\,\text{nm}$, and are placed on one-monolayer thick wetting layer. Both the existence of the wetting layer and the larger radius of the top disk are commonly seen in the fabricated double-dot samples [4,5]. We also attempt to approximate the experimental system by our selection of the boundary conditions in the strain calculation: we assume that the atomic positions become fixed to the bulk lattice coordinates at the distance of 55.4 nm below the dots, and that the system is covered by a 37.7-nm thick GaAs cap, whose top surface can distort freely. In the lateral direction we assume periodic boundary conditions. The computational procedure applied to our system first involves the computation of strain in a computational domain large enough to account for the long-range character of the displacement field (typically it contains up to 60 million atoms). However, the electronic structure calculations are carried out on a smaller domain, typically containing up to 20 million atoms, since the wave functions of confined orbitals decay exponentially in the barrier. The resulting Hamiltonian matrix is of order of $\sim 10^8$ and is diagonalized using the Lanczos algorithm. Fig. 3(a) shows the electron energies, and Fig. 3(b) shows the hole energies obtained in this approach as a function of D. As it can be seen, the bonding and antibonding behavior of the electron energies is not destroyed by the explicit breaking of symmetry of the system, which is reflected by the shared probability distribution in the electronic ground and first excited state presented in the left-hand part of Fig. 3(a). However, in contrast to the previous results the shells do not become degenerate at large interdisk distances D. This is a consequence of the difference in QD radii, making the ground state energy of the isolated bottom dot higher than that of the top dot (see the right-hand part of Fig. 3(a)). As

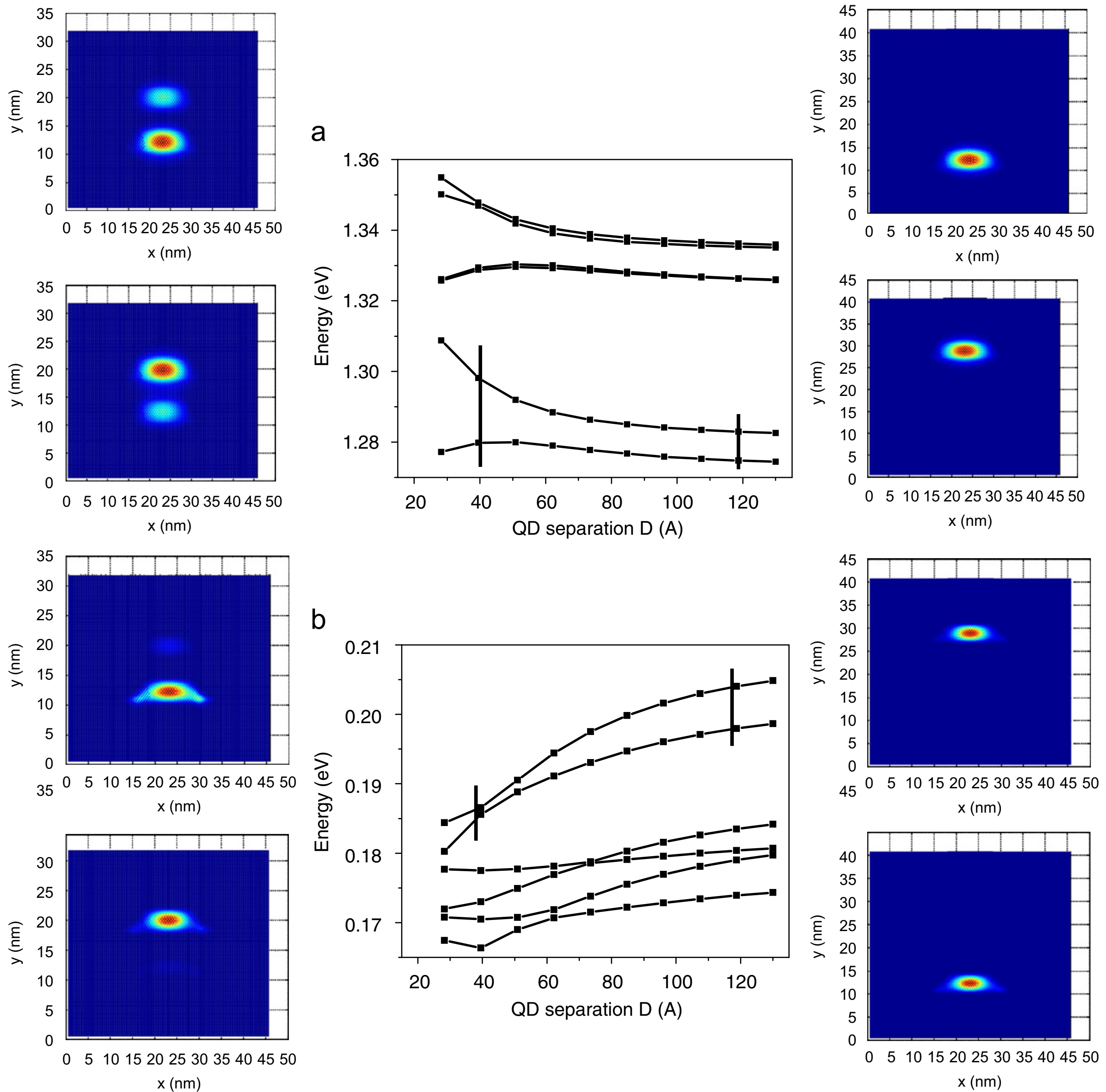

Fig. 3. Electron (a) and hole (b) energies of the double-dot molecule as a function of the distance D between the dots calculated using the $sp^3d^5s^*$ atomistic approximation with the NEMO3D simulator. Diagrams on the left- and right-hand sides show the probability density of selected states at separations D marked in energy diagrams with vertical lines.

for the hole energies, in Fig. 3(b) we can distinguish two families of curves: one with a larger and one with a smaller slope. These families can be identified with molecular orbitals localized in respective dots, with the ground state localized predominantly in the large dot at large D, as seen in probability distributions in the right-hand part of Fig. 3(b). Note, however, that at $D \leqslant 4$ nm the two energy levels cross. At a slightly smaller D the ground hole state appears to correspond to the orbital localized predominantly on the smaller dot, as seen in the probability diagrams on the left-hand side of Fig. 3(b). The reason for that behavior lies in the amount of strain experienced by the lower dot at small D. The lack of symmetry of the system, introduced by the different boundary conditions on the top and bottom of the strain computational domain, leads to a greater amount of strain in the bottom dot compared to that in the top dot. This leads to an additional increase in confinement depth, which, in this case, overcomes the effect of the size disparity.

The strain-induced asymmetry was studied additionally in the system of a seven-dot molecule composed of identical QDs of radius $R = 6.5$ nm and height $H = 2.5$ nm, each positioned on a one-monolayer thick wetting layer. The distance D between adjacent dots was set to 4 nm. In Fig. 4 we show the cross-section of the probability density of the seven lowest electronic orbitals. These orbitals form a miniband of s-type states, and differ by the vertical symmetry—from the nodeless ground state

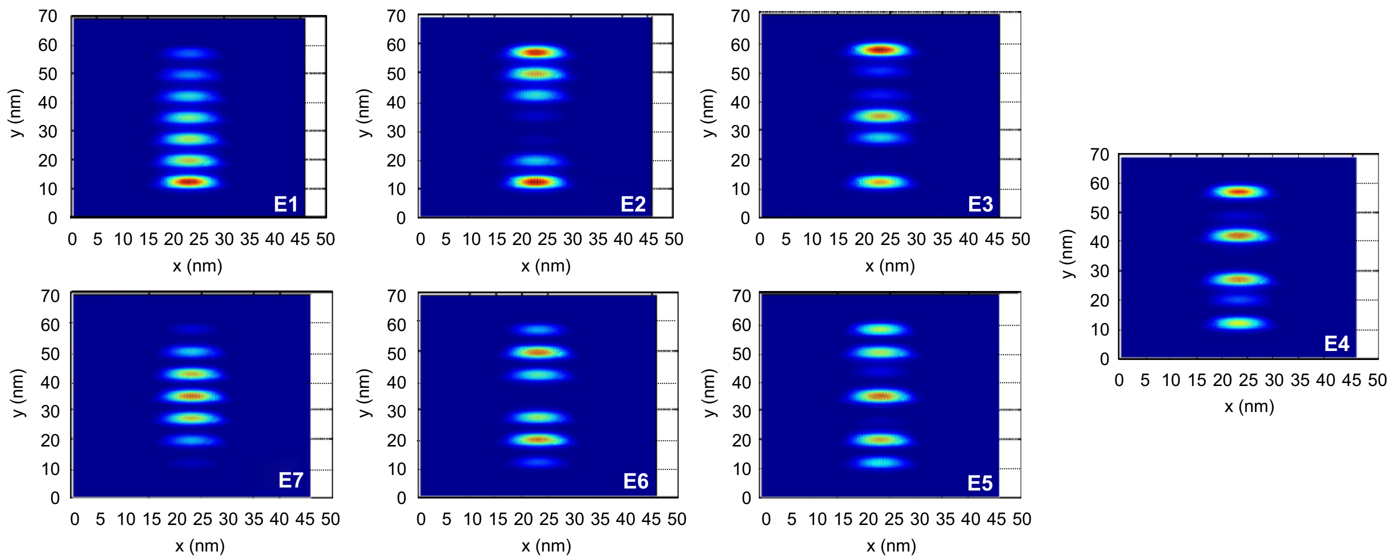

Fig. 4. Probability densities of the seven lowest electronic orbitals confined in a seven-dot artificial molecule. The orbitals are ordered with increasing energy clockwise from the lowest ($E1$) to the highest ($E7$).

to the seventh state exhibiting six nodes. Note that the states with low energies are not fully symmetric, with a larger probability density at the bottom of the structure. In the higher lying states, however, the effects of strain-induced asymmetry are no longer apparent, and the highest state $E7$ appears to be fully symmetric.

References

[1] P. Hawrylak, M. Korkusinski, Single quantum dots: fundamentals, applications, and new concepts, in: P. Michler (Ed.), Topics in Applied Physics, vol. 90, Springer, Berlin, 2003.
[2] L. Jacak, P. Hawrylak, A. Wojs, Quantum Dots, Springer, Berlin, 1998.
[3] D. Bimberg, M. Grundmann, N.N. Ledentsov, Quantum Dot Heterostructures, Wiley, New York, 1998.
[4] S. Fafard, M. Spanner, J.P. McCaffrey, Z.R. Wasilewski, Appl. Phys. Lett. 76 (2000) 2268.
[5] M. Bayer, P. Hawrylak, K. Hinzer, S. Fafard, M. Korkusinski, Z. Wasilewski, O. Sterna, A. Forchel, Science 291 (2001) 451.
[6] H.J. Krenner, E.C. Clark, T. Nakaoka, M. Bichler, C. Scheurer, G. Abstreiter, J.J. Finley, Phys. Rev. Lett. 97 (2006) 076403.
[7] B.D. Gerardot, S. Strauf, M.J.A. de Dood, A.B. Bychkov, A. Badolato, K. Hennessy, E.L. Hu, D. Bouwmeester, P.M. Petroff, Phys. Rev. Lett. 95 (2005) 137403.
[8] M. Bayer, O. Stern, P. Hawrylak, S. Fafard, A. Forchel, Nature (London) 405 (2000) 923;
P. Hawrylak, Phys. Rev. B 60 (1999) 5597.
[9] P. Hawrylak, G.A. Narvaez, M. Bayer, A. Forchel, Phys. Rev. Lett. 85 (2000) 389.
[10] A. Hartmann, Y. Ducommun, E. Kapon, U. Hohenester, E. Molinari, Phys. Rev. Lett. 84 (2000) 5648.
[11] H. Drexler, D. Leonard, W. Hansen, J.P. Kotthaus, P.M. Petroff, Phys. Rev. Lett. 73 (1994) 2252.
[12] A. Babinski, M. Potemski, S. Raymond, J. Lapointe, Z.R. Wasilewski, Phys. Rev. B 74 (2006) 155301;
S.-J. Cheng, W. Sheng, P. Hawrylak, Phys. Rev. B 68 (2005) 235330.
[13] J.J. Finley, M. Sabathil, P. Vogl, G. Abstreiter, R. Oulton, A.I. Tartakovskii, D.J. Mowbray, M.S. Skolnick, S.L. Liew, A.G. Cullis, M. Hopkinson, Phys. Rev. B 70 (2004) 201308.
[14] G. Klimeck, F. Oyafuso, T.B. Boykin, R.C. Bowen, P. von Allmen, Comput. Model. Eng. Sci. 3 (2002) 601.
[15] M. Bayer, G. Orther, O. Stern, A. Kuther, A.A. Gorbunov, A. Forchel, P. Hawrylak, S. Fafard, K. Hinzer, T.L. Reinecke, S.N. Walck, J.P. Reithmaier, F. Klopf, F. Schäfer, Phys. Rev. B 65 (2002) 195315;
J.J. Finley, D.J. Mowbray, M.S. Skolnick, A.D. Ashmore, C. Baker, A.F.G. Monte, Phys. Rev. B 66 (2002) 153316;
A. Högele, S. Seidl, M. Kroner, K. Karrai, R.J. Warburton, B.D. Gerardot, P.M. Petroff, Phys. Rev. Lett. 93 (2004) 217401.
[16] A. Babinski, G. Ortner, S. Raymond, M. Potemski, M. Bayer, W. Sheng, P. Hawrylak, Z. Wasilewski, S. Fafard, A. Forchel, Phys. Rev. B 74 (2006) 075310;
W. Sheng, A. Babinski, Phys. Rev. B 75 (2007) 033316.
[17] M. Bayer, A. Kuther, A. Forchel, A. Gorbunov, V.B. Timofeev, F. Schäfer, J.P. Reithmaier, T.L. Reinecke, S.N. Walck, Phys. Rev. Lett. 82 (1999) 1748.
[18] G. Bester, A. Zunger, Phys. Rev. B 71 (2005) 045318.
[19] L. He, G. Bester, A. Zunger, Phys. Rev. B 72 (2005) 081311.
[20] W. Jaskólski, M. Zieliński, G.W. Bryant, J. Aizpurua, Phys. Rev. B 74 (2006) 195339.
[21] H.J. Krenner, M. Sabathil, E.C. Clark, A. Kress, D. Schuh, M. Bichler, G. Abstreiter, J.J. Finley, Phys. Rev. Lett. 94 (2005) 057402;
I. Shtrichman, C. Metzner, B.D. Gerardot, W.V. Schoenfeld, P.M. Petroff, Phys. Rev. B 65 (2002) 081303.
[22] G. Bester, A. Zunger, J. Shumway, Phys. Rev. B 71 (2005) 075325;
L. He, A. Zunger, Phys. Rev. B 75 (2007) 075330.
[23] C. Pryor, Phys. Rev. Lett. 80 (1998) 3579.
[24] C. Pryor, J. Kim, L.W. Wang, A.J. Williamson, A. Zunger, J. Appl. Phys. 83 (1998) 2548;
M. Tadić, F.M. Peeters, K.L. Janssens, M. Korkusinski, P. Hawrylak, J. Appl. Phys. 92 (2002) 5819.
[25] P.N. Keating, Phys. Rev. 145 (1966) 637;
R.M. Martin, Phys. Rev. B 1 (1970) 4005.
[26] M. Grundmann, O. Stier, D. Bimberg, Phys. Rev. B 52 (1995) 11969.
[27] M. Korkusinski, G. Klimeck, J. Phys. Conf. Ser. 38 (2006) 75.
[28] P. Vogl, H.P. Hjalamarson, J.D. Dow, J. Phys. Chem. Solids 44 (1983) 365.
[29] J.C. Slater, G.F. Koster, Phys. Rev. 94 (1954) 1498.
[30] W.A. Harrison, Elementary Electronic Structure, World Scientific, Singapore, 1999.

[31] J.M. Jancu, R. Scholz, F. Beltram, F. Bassani, Phys. Rev. B 57 (1998) 6493.
[32] G. Klimeck, R.C. Bowen, T.B. Boykin, T.A. Cwik, Superlattice Microstruct. 27 (2000) 519.
[33] G. Klimeck, F. Oyafuso, T.B. Boykin, R.C. Bowen, P. von Allmen, Comput. Model. Eng. Sci. 3 (2002) 601;
F. Oyafuso, G. Klimeck, R.C. Bowen, T.B. Boykin, J. Comput. Electronics 1 (2002) 317.
[34] J.G. Diaz, G.W. Bryant, Phys. Rev. B 73 (2006) 075329.
[35] S. Lee, F. Oyafuso, P. von Allmen, G. Klimeck, Phys. Rev. B 69 (2004) 045316.
[36] Y.-C. Chang, Phys. Rev. B 37 (1988) 8215;
S.J. Sun, Y.-C. Chang, Phys. Rev. B 62 (2000) 13631;
J.P. Loehr, Phys. Rev. B 50 (1994) 5429;
W. Sheng, S.-J. Cheng, P. Hawrylak, Phys. Rev. B 71 (2005) 035316.
[37] W. Sheng, J.P. Leburton, Phys. Rev. Lett. 88 (2002) 167401;
A. Schliwa, O. Stier, R. Heitz, M. Grundmann, D. Bibmberg, Phys. Status Solidi B 224 (2001) 405;
M. Tadić, F.M. Peeters, B. Partoens, K.L. Janssens, Physica E 13 (2002) 237.
[38] M. Korkusinski, P. Hawrylak, Phys. Rev. B 63 (2001) 195311.
[39] C. Pryor, Phys. Rev. B 57 (1998) 7190.
[40] M. Korkusinski, W. Sheng, P. Hawrylak, Z. Wasilewski, G. Ortner, M. Bayer, A. Babinski, M. Potemski, Physics of semiconductors, in: Proceedings of the 27th ICPS, 2005, p. 685.